

Exploring parameter dependence of atomic minima with implicit differentiation

Ivan Maliyov,^{1,*} Petr Grigorev,¹ and Thomas D Swinburne^{1,†}

¹*Aix-Marseille Université, CNRS, CINaM UMR 7325, Campus de Luminy, Marseille 13288, France*

Interatomic potentials are essential to go beyond *ab initio* size limitations, but simulation results depend sensitively on potential parameters. Forward propagation of parameter variation is key for uncertainty quantification, whilst backpropagation has found application for emerging inverse problems such as fine-tuning or targeted design. Here, the implicit derivative of functions defined as a fixed point is used to Taylor-expand the energy and structure of atomic minima in potential parameters, evaluating terms via automatic differentiation, dense linear algebra or a sparse operator approach. The latter allows efficient forward and backpropagation through relaxed structures of arbitrarily large systems. The implicit expansion accurately predicts lattice distortion and defect formation energies and volumes with classical and machine-learning potentials, enabling high-dimensional uncertainty propagation without prohibitive overhead. We then show how the implicit derivative can be used to solve challenging inverse problems, minimizing an implicit loss to fine-tune potentials and stabilize solute-induced structural rearrangements at dislocations in tungsten.

I. INTRODUCTION

Atomic simulations employing interatomic potentials are an essential tool of computational materials science [1]. Classical models such as Lennard-Jones potentials are central to the study of glasses and polymer systems, whilst modern, data-driven models are becoming quantitative surrogates for *ab initio* calculations [2]. For solid-state materials, the energy landscape of relaxed atomic geometries is central to exploring thermodynamic, diffusive and mechanical properties [3–6].

Regardless of the interatomic potential employed, changing parameters will change any quantity of interest extracted from a simulation. For simple classical models, parameter variation is essential to explore the model’s phenomenology [5, 7]. For modern data-driven models that target quantitative accuracy, parameter uncertainties can be estimated by Bayesian regression on training data [8, 9] and should be forward-propagated to simulation results to bound quantities of interest [10–13].

Backpropagation of structural modifications to changes in parameters is finding application in inverse material design [14, 15], training interatomic potentials from experimental data [16], or ‘fine-tuning’ simple interatomic potentials to reproduce desired self-assembly kinetics [7]. More recently, ‘universal’ machine learning potentials have shown near-quantitative accuracy across large portions of the periodic table [17, 18]. This has raised interest in backpropagation for fine-tuning universal models for specific applications [19], and opened the possibility of targeted design through navigation of a smooth latent composition representation [20].

Forward and backpropagation of parameter variation through complex simulations is typically achieved using

reverse-mode automatic differentiation (AD) routines, which offer high arithmetic efficiency at the price of large memory requirements [21–24]. Whilst AD offers clear advantages in implementation, their significant memory burden complicates application to large atomic systems, especially when targeting higher derivatives beyond forces. Existing methods to propagate variation in parameters to variation in simulation results thus typically employ resampling: new parameters are drawn from some distribution [10] and simulations are repeated. Whilst conceptually straightforward, backpropagation is not possible, assessing convergence is challenging, and the cost can be potentially very large, especially for simulation results requiring geometry minimization for each potential sample.

In this paper, we explore an alternative approach, analytically expanding the structure of relaxed minima to first order in parameter variation, giving a second order expansion of the total energy. The expansion is achieved through evaluation of an *implicit* derivative [25], i.e. the derivative of a function defined as fixed point, in this case, the atomic structure of a local minimum (Fig. 1a). Our main results are that the implicit derivative enables 1) forward propagation of parameter uncertainties to simulation results for orders of magnitude less computational effort than resampling schemes, allowing rapid propagation of parameter uncertainties and 2) backpropagation of structural variations to target composition-induced structural rearrangements in multi-thousand-atom systems, a challenging task for any other approach (see illustration of these two ideas in Fig. 1b and 1c).

We implement and compare methods to evaluate the implicit derivative using AD [22, 23], dense linear algebra and a sparse operator approach, using the `jax-md` [21] and LAMMPS [26] simulation codes. We find AD routines for the implicit derivative reach GPU memory limits for ~ 1000 -atom systems even on best-in-class hardware. In contrast, the sparse operator technique reduces to a constrained minimization in LAMMPS, allowing memory-efficient and highly parallelized evaluation. Our devel-

* ivan.maliyov@cnrs.fr

† thomas.swinburne@cnrs.fr

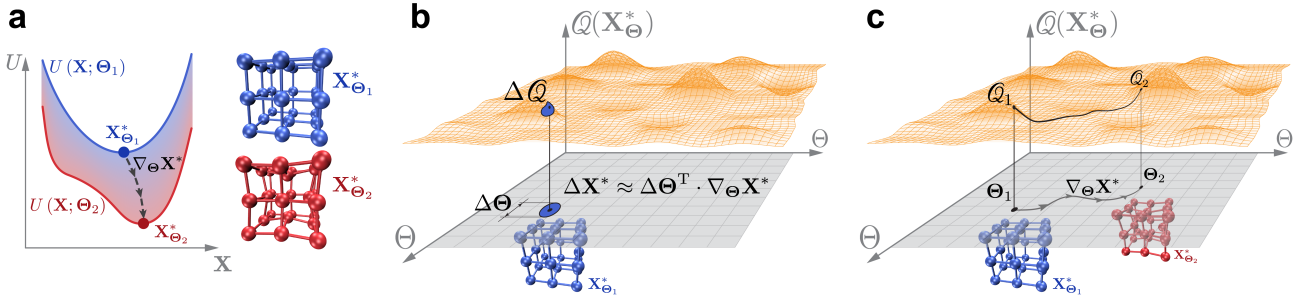


FIG. 1. **Schematic of the implicit derivative approach in atomic systems.** **a** A local minimum \mathbf{X}_{Θ}^* will change under changes in potential parameters Θ . The implicit derivative is the gradient of this change, allowing a first-order prediction of structural variations and a second-order prediction of energy variations. **b** Uncertainty quantification application. Having the uncertainty in the parameter space, $\Delta\Theta$, implicit derivative allows one to compute the uncertainty of any molecular statics property Q . **c** Inverse design application. With initial configuration $\mathbf{X}_{\Theta_1}^*$ and potential Θ_1 , one defines a target configuration $\mathbf{X}_{\Theta_2}^*$. Implicit derivative allows one to effectively minimize the potential parameters that provide the target configuration.

oped approach enables uncertainty quantification and inverse design studies with the large atomic simulations essential to capture realistic defect structures.

For the purposes of backpropagation, our expansion can be used for any form of interatomic potential. However, for the forward propagation in uncertainty quantification, the expansion captures parameter variation in the vicinity of some minimum of the loss. In this paper we therefore focus on classical [21, 27, 28] and linear-in-descriptor interatomic potentials [8, 29–32] whose loss typically has a well defined global minimum rather than the multi-modal loss landscape of neural network potentials [5, 17, 33].

The paper is structured as follows. We first define the implicit derivative, the Taylor expansion approximations used and their evaluation using automatic differentiation or linear algebra techniques. We then describe how the implicit derivative can be used in forward and backpropagation of parameter variations. Forward propagation of parameter variation is demonstrated using classical and machine learning potentials to explore lattice distortion and vacancy defect formation [34]. Finally, we apply the implicit derivative approach to the inverse material design problems, finding parameter variations that stabilize subtle solute-induced dislocation core reconstructions in tungsten [4].

II. RESULTS

A. Implicit derivative of atomic configurations

We consider a system of N atoms in a periodic supercell of volume V , with atomic coordinates $\mathbf{X} \in \mathbb{R}^{N \times 3}$ and a supercell matrix $\mathbf{C} \in \mathbb{R}^{3 \times 3}$, $V = \det(\mathbf{C})$. Changes to the supercell $\mathbf{C} \rightarrow \mathbf{C} + \delta\mathbf{C}$ are defined to induce homogeneous deformations, as in e.g. energy volume curves. We then define scaled atomic coordinates $\tilde{\mathbf{X}}$, such that $\mathbf{X} \equiv \tilde{\mathbf{X}}\mathbf{C}$ and the tuple $(\tilde{\mathbf{X}}, \mathbf{C})$ fully describes atomic

configurations with periodic boundary conditions. With a vector of N_D potential parameters Θ , a potential energy model $U(\tilde{\mathbf{X}}, \mathbf{C}; \Theta)$, has stationary configurations $(\tilde{\mathbf{X}}_{\Theta}^*, \mathbf{C}_{\Theta}^*)$ satisfying

$$\nabla_{\tilde{\mathbf{X}}} U(\tilde{\mathbf{X}}_{\Theta}^*, \mathbf{C}_{\Theta}^*; \Theta) \equiv 0, \quad \nabla_{\mathbf{C}} U(\tilde{\mathbf{X}}_{\Theta}^*, \mathbf{C}_{\Theta}^*; \Theta) \equiv 0 \quad (1)$$

where $(\tilde{\mathbf{X}}_{\Theta}^*, \mathbf{C}_{\Theta}^*)$ is one of the exponentially many stationary points in the energy landscape [5]. In the following, we only consider minima; extension to the treatment of saddle points will be presented in future work. Under a parameter variation $\Theta + \delta\Theta$ the scaled positions and supercell matrix are defined to change as

$$\tilde{\mathbf{X}}_{\Theta+\delta\Theta}^* = \tilde{\mathbf{X}}_{\Theta}^* + \delta\Theta \nabla_{\Theta} \tilde{\mathbf{X}}_{\Theta}^* + \mathcal{O}(\delta\Theta^2), \quad (2)$$

$$\mathbf{C}_{\Theta+\delta\Theta}^* = \mathbf{C}_{\Theta}^* + \delta\Theta \nabla_{\Theta} \mathbf{C}_{\Theta}^* + \mathcal{O}(\delta\Theta^2), \quad (3)$$

where $\nabla_{\Theta} \tilde{\mathbf{X}}_{\Theta}^* \in \mathbb{R}^{N_D \times N \times 3}$ and $\nabla_{\Theta} \mathbf{C}_{\Theta}^* \in \mathbb{R}^{N_D \times 3 \times 3}$ are *implicit* derivatives that determine how a *stationary* configuration changes with the variation of potential parameters. In practical applications, supercell variation \mathbf{C} is typically constrained; for simplicity, we will only consider fixed-volume simulations or isotropic variations controlled by a homogeneous strain $\epsilon_{\Theta}^* \in \mathbb{R}$ around a reference supercell \mathbf{C}_0

$$\mathbf{C}_{\Theta}^* = [1 + \epsilon_{\Theta}^*] \mathbf{C}_0, \quad \nabla_{\Theta} \mathbf{C}_{\Theta}^* = (\nabla_{\Theta} \epsilon_{\Theta}^*) \mathbf{C}_0, \quad (4)$$

where $\nabla_{\Theta} \epsilon_{\Theta}^* \in \mathbb{R}^{N_D}$. Taylor-expanding equations (1) to first order in $\delta\Theta$, it is simple to show that $\nabla_{\Theta} \tilde{\mathbf{X}}_{\Theta}^*, \nabla_{\Theta} \epsilon_{\Theta}^*$ solve the system of linear equations

$$[\nabla_{\Theta} \tilde{\mathbf{X}}_{\Theta}^* \quad \nabla_{\Theta} \epsilon_{\Theta}^*] \begin{bmatrix} \nabla_{\tilde{\mathbf{X}}\tilde{\mathbf{X}}}^2 U & \nabla_{\tilde{\mathbf{X}}\epsilon}^2 U \\ \nabla_{\tilde{\mathbf{X}}\epsilon}^2 U^T & \nabla_{\epsilon\epsilon}^2 U \end{bmatrix} = - \begin{bmatrix} \nabla_{\Theta\tilde{\mathbf{X}}}^2 U \\ \nabla_{\Theta\epsilon}^2 U \end{bmatrix}, \quad (5)$$

where $\nabla_{\tilde{\mathbf{X}}\tilde{\mathbf{X}}}^2 U$ is the Hessian matrix in scaled coordinates, $\nabla_{\epsilon\epsilon}^2 U$ is proportional to the bulk modulus of the system, $-\nabla_{\tilde{\mathbf{X}}\epsilon}^2 U$ is proportional to change in atomic forces under a homogeneous strain and $\nabla_{\Theta\tilde{\mathbf{X}}}^2 U, \nabla_{\Theta\epsilon}^2 U$ are mixed curvatures. Whilst the solution of (5) in

principle requires $\mathcal{O}(N^3)$ effort due to the Hessian, we introduce a Hessian-free solution method below, allowing application to large systems.

B. Taylor expansion of stationary energies and volumes using implicit derivatives

In our numerical experiments, we will compare three levels of approximate solution to the linear equations (5):

- *constant (c)*: $\nabla_{\Theta}\epsilon_{\Theta}^* = 0$, $\nabla_{\Theta}\tilde{\mathbf{X}}_{\Theta}^* = \mathbf{0}$
- *homogeneous (h)*: $\nabla_{\Theta}\epsilon_{\Theta}^* \neq 0$, $\nabla_{\Theta}\tilde{\mathbf{X}}_{\Theta}^* = \mathbf{0}$
- *inhomogeneous (ih)*: $\nabla_{\Theta}\epsilon_{\Theta}^* = 0$, $\nabla_{\Theta}\tilde{\mathbf{X}}_{\Theta}^* \neq \mathbf{0}$,

with the full expansion then given the shorthand $h+ih$. Under changes in parameters Θ , changes in the stationary energy and volume (or equivalently strain) admit the implicit Taylor expansions

$$\delta^{(\zeta)}U^* \equiv \delta\Theta\nabla_{\Theta}U + \delta\Theta\mathbf{H}_{\zeta}\delta\Theta^{\top} + \mathcal{O}(\delta\Theta^3) \quad (6)$$

$$\delta^{(\zeta)}\epsilon^* \equiv \delta\Theta\nabla_{\Theta}\epsilon_{\zeta}^* + \mathcal{O}(\delta\Theta^2), \quad (7)$$

where $\mathbf{H}_{\zeta} \in \mathbb{R}^{N_D \times N_D}$ is a generalized curvature within a given level of approximation and $\zeta = c, h, ih, h+ih$ is the level of approximation used. Expressions for $\nabla_{\Theta}\epsilon_{\zeta}^*$ and \mathbf{H}_{ζ} are given in the supplementary material.

In all three approaches, the potential parameters Θ vary; therefore, each method predicts changes in energy. However, only $\zeta = h, ih, h+ih$ predict changes in structure. For constant volume relaxations, the inhomogeneous $\zeta = ih$ expansion is asymptotically exact. For variable volume relaxations, the full $\zeta = h+ih$ expansion is asymptotically exact, but as we show below, the cheaper homogeneous $\zeta = h$ expansion can also give accurate results when the focus is on changes to the energy or volume, rather than structure.

C. Evaluation of the implicit derivative through sparse and dense linear algebra methods

In the linear equations (5), the $\nabla_{\epsilon\epsilon}^2U$ and $\nabla_{\epsilon\tilde{\mathbf{X}}}^2U$ derivatives require only a few $\mathcal{O}(N)$ force calls for evaluation. As a result, the *homogeneous* approximation requires minimal computational effort, but all knowledge of structural changes is missing as $\nabla_{\Theta}\tilde{\mathbf{X}}^*$ is not evaluated. Evaluation of $\nabla_{\Theta}\tilde{\mathbf{X}}^*$ for the *inhomogeneous* approach requires $\mathcal{O}(N^2)$ finite difference evaluations of the Hessian matrix $\nabla_{\tilde{\mathbf{X}}\tilde{\mathbf{X}}}^2U$ and $\mathcal{O}(N^3)$ solution of the dense linear equation (5). Whilst of reasonable cost for small systems ($N < 2000$), study of extended defects where $10^4 < N < 10^6$ requires significant, typically prohibitive, computational resources and careful use of shared memory parallel linear algebra techniques [6].

To overcome this limitation, we note that the Hessian matrix is highly sparse due to the strong locality of atomic forces. In this regime, efficient solutions of the linear equations (5) can be obtained using iterative algorithms. In addition, such algorithms do not require access to every element of the Hessian at each iteration, only a linear operator that gives the action of the Hessian on some vector $\mathbf{V} \in \mathbb{R}^{N \times 3}$, i.e. $\mathcal{L}(\mathbf{V}) = \mathbf{V}\nabla_{\tilde{\mathbf{X}}\tilde{\mathbf{X}}}^2U$.

Avoiding direct Hessian evaluation can give a much faster time-to-solution. We define the operator

$$\mathcal{L}(\mathbf{V}) \equiv \lim_{\alpha \rightarrow 0} \nabla_{\tilde{\mathbf{X}}}U(\tilde{\mathbf{X}}_{\Theta}^* + \alpha\mathbf{V}, \mathbf{C}_{\Theta}^*; \Theta)/\alpha, \quad (8)$$

which, in the limit, is equal to $\mathcal{L}(\mathbf{V}) = \mathbf{V}\nabla_{\tilde{\mathbf{X}}\tilde{\mathbf{X}}}^2U$ as desired and only requires $\mathcal{O}(N)$ force calls for evaluation. To compute the *inhomogeneous* implicit derivative, we apply the sparse linear operator to each vector $[\nabla_{\Theta}\tilde{\mathbf{X}}_{\Theta}^*]_l \in \mathbb{R}^{N \times 3}$, $l \in [1, N_D]$. Details of our $\mathcal{O}(NN_D)$ massively parallel method to compute $\nabla_{\Theta}\tilde{\mathbf{X}}^*$ in LAMMPS [26] at finite values of α is described in methods section IV A. In section II H, we apply the method to enable the use of the implicit derivative in large atomic systems.

D. Evaluation of the implicit derivative with automatic differentiation methods

AD-enabled simulation schemes such as `jax-md` [21] can clearly evaluate all terms in equation (5) or the sparse operator approach (8). Recently, implicit differentiation schemes have been implemented in `jaxopt` [22, 23], allowing direct evaluation of e.g., $\nabla_{\Theta}\tilde{\mathbf{X}}^*$ by differentiating through the minimization algorithm chosen in `jax-md`. We have implemented and tested all approaches in AD for the binary Lennard-Jones system described below. Despite the simplicity of the potential form, using AD implicit derivative schemes incurs extremely large memory usage, reaching the 80GB limit on NVIDIA A100 GPUs for only a few thousand atoms, as we detail in the supplementary material. We thus conclude that existing AD schemes for direct evaluation of the implicit derivative or Hessian matrices are ill-suited for application to the thousand-atom systems essential for many materials science problems. In contrast, our sparse operator technique has the same memory usage as any structural minimization. Whilst still incurring a significantly greater memory burden than non-AD methods implemented in LAMMPS, our sparse operator is ideal for implicit derivative evaluation in AD-enabled schemes.

E. Backpropagation of parameter variations for inverse design problems

Inverse design aims to produce materials with specified (desirable) properties through inverting structure-property relationships. However, this typically requires

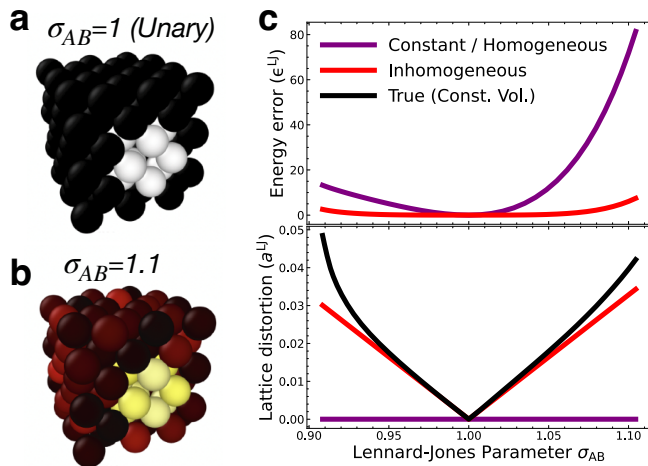


FIG. 2. **Automatic implicit differentiation with classical potentials.** **a, b** Atomic configurations of a single vacancy configuration with $\sigma_{AB} = 1$ (unary) and $\sigma_{AB} = 1.1$ (random binary). Atom colors encode fcc centrosymmetry in the range $[0, 1.25]$; black color corresponds to perfect fcc structure. **c** Relaxed energy and lattice distortion for $\sigma_{AB} \in [0.9, 1.1]$ at fixed volume. The true values are obtained with the energy minimization at each σ_{AB} value.

high-throughput searches, which necessarily cannot afford to perform atomistic simulations of e.g. defect structures and mechanisms to predict mechanical properties. The implicit derivative can be used to make a first step toward gradient-led inverse design, allowing us to find interatomic parameters Θ that stabilise some atomic configuration $\mathbf{X}_{\text{ref}}^*$ observed in an *ab initio*-accurate simulation e.g. using the density-functional theory (DFT) [4]. We define an implicit loss function:

$$L(\Theta) = \frac{1}{2} \|\mathbf{X}_{\Theta}^* - \mathbf{X}_{\text{ref}}^*\|^2. \quad (9)$$

To effectively minimize the loss, the loss gradient is required, and the implicit derivative is necessary to compute the derivative of the loss via the chain rule:

$$\nabla_{\Theta} L(\Theta) = \nabla_{\Theta} \mathbf{X}_{\Theta}^* \cdot [\mathbf{X}_{\Theta}^* - \mathbf{X}_{\text{ref}}^*] \in \mathbb{R}^{N_D}. \quad (10)$$

An immediate application of the implicit loss, equation (9), is the ability to ‘fine-tune’, or retrain [4], interatomic potentials to reproduce important DFT minima. Fine-tuning has gained increasing interest following the rise of ‘universal’ machine learning potentials [18]. In practice, one typically includes the loss against the original training database to regularize the fine-tuning fit. However, we have found that minimizing (9) in practice produces only very small perturbations to the final potential.

The ability to fine-tune interactions is of particular relevance for low energy structures such as dislocation lines [4, 8], which typically require careful weighting in potential fitting [18]. In section IIH, we use implicit loss minimization to find solute substitutions which induce ‘hard’ screw dislocation core reconstruction in tungsten,

and fine-tune a tungsten-beryllium potential to correctly reproduce *ab initio* observations.

F. Prediction of the total relaxed energy in classical potentials with automatic differentiation

The binary Lennard-Jones potential is a classical model for nanoclusters and glassy systems [5]. The model is defined by six parameters, $\Theta = [\epsilon_{AA}^{\text{LJ}}, \epsilon_{AB}^{\text{LJ}}, \epsilon_{BB}^{\text{LJ}}, \sigma_{AA}, \sigma_{AB}, \sigma_{BB}]$, with a total energy

$$U(\tilde{\mathbf{X}}, \mathbf{C}; \Theta) = \sum_i \sum_{j \in N_i} \epsilon_{s_i s_j}^{\text{LJ}} \left(\frac{\sigma_{s_i s_j}^{12}}{r_{ij}^{12}} - \frac{\sigma_{s_i s_j}^6}{r_{ij}^6} \right), \quad (11)$$

where s_i is species i , $s_i \in [A, B]$, r_{ij} is the minimum image distance (as determined by **C**) between atoms i, j and N_i is the set of neighbors of i . As discussed above, automatic differentiation enabled by `jax-md` was used to study this simple system, with all examples shown using the dense linear algebra approach to evaluate the implicit derivative at constant volume.

To simplify the problem, we set $\epsilon_{AA}^{\text{LJ}} = \epsilon_{AB}^{\text{LJ}} = \epsilon_{BB}^{\text{LJ}}$ and $\sigma_{AA} = \sigma_{BB} = 1$, leaving $\Theta = \sigma_{AB}$ as the only varying parameter in this example. When $\sigma_{AB} = 1$, all atoms are identical and the system is a unary fcc lattice; we additionally remove one atom to form a vacancy and promote additional deformation. When $\sigma_{AB} \neq 1$ the system becomes a random fcc binary alloy, with lattice distortion in the bulk and around the vacancy (see Fig. 2a and 2b). Figure 2c shows the *inhomogeneous* implicit derivative around $\sigma_{AB} = 1$ that gives an excellent prediction of the total energy and lattice distortion for $\sigma_{AB} \in [0.95, 1.05]$, with mild disagreement as $|\sigma_{AB} - 1|$ grows. At constant volume, both *constant* and *homogeneous* approximations are equivalent and predict no structural change, with significantly higher errors. In the remainder of this paper, we focus on modern machine learning potentials.

G. Prediction of defect formation energies and volumes with machine learning potentials

Almost all modern interatomic models use high-dimensional regression techniques from the machine learning community [8, 18, 35, 36]. A common first step is to represent atomic environments as N_D per-atom descriptor functions $D_l(\tilde{\mathbf{X}}, \mathbf{C}, i)$, $l \in [1, N_D]$ which describe the atomic environment around an atom of index i . In practice, the descriptor functions also have species-dependent hyperparameters which must also be tuned, but in the following, we assume that these are fixed. We use the widely implemented SNAP Bispectrum descriptors [29] with $N_D = 55$ (see methods, section IV C, for multi-specie generalization), giving a potential energy

$$U(\tilde{\mathbf{X}}, \mathbf{C}; \Theta) = \Theta \sum_i \mathbf{D}(\tilde{\mathbf{X}}, \mathbf{C}, i) \equiv \Theta \cdot \mathbf{D}(\tilde{\mathbf{X}}, \mathbf{C}), \quad (12)$$

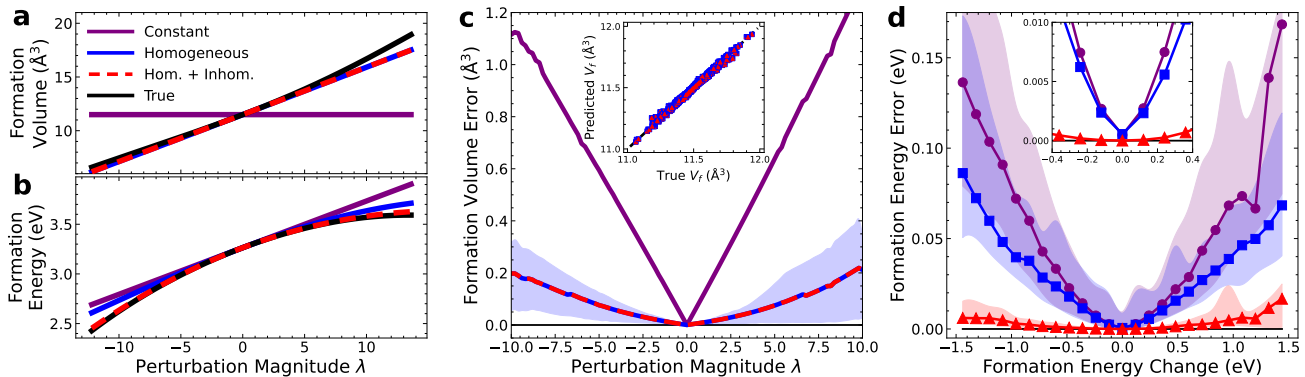


FIG. 3. **Implicit differentiation of vacancy defect formation with SNAP potentials.** **a, b** Formation volume and formation energy vs potential perturbation magnitude for one of 100 tungsten potential samples used in the study. **c** Average absolute error of formation volume vs perturbation magnitude. On the inset, predicted vacancy formation volume vs its true value obtained with the full relaxation. **d** Error vs change in vacancy formation energy averaged over the set of potentials and perturbation magnitudes. On the inset, zoom into a smaller formation energy range. In **c,d** the shaded regions indicates the [16%, 84%] percentile ($\pm 1\sigma$) range across all parameter variations. Line colors across the panels indicate the prediction method with the legend presented in **a**. In **d**, symbols are added at data points. Pristine supercell size of 128 atoms was used in the study.

where $\Theta \in \mathbb{R}^{N_D}$ is the potential parameter vector and $\mathbf{D}(\mathbf{X}, \mathbf{C}) \in \mathbb{R}^{N_D}$ is the total descriptor vector. The advantage of the linear functional form is that $\nabla_{\Theta} U = \mathbf{D}$ and $\nabla_{\Theta \mathbf{X}}^2 U = \nabla_{\mathbf{X}} \mathbf{D}$, required for the solution of equation (5), are readily evaluated without any numerical or automatic differentiation schemes.

For multi-scale uncertainty quantification study, we use DFT training data for tungsten from Goryaeva *et al.* [8] and generate 100 samples Θ_m (m is a sample index) from a parameter distribution using the approach described in [9]. We are primarily interested in using the variations of parameter samples away from the reference potential $\bar{\Theta}$ to test our implicit expansion method. To this end, we define an additional ‘perturbation magnitude’ λ and generate samples with

$$\Theta(\lambda, m) = \bar{\Theta} + \lambda(\Theta_m - \bar{\Theta}), \quad (13)$$

such that $\lambda = 0$ corresponds to the reference potential $\bar{\Theta}$ and $\lambda = 1$ corresponds to the original sample Θ_m . We then generate very large (and thus sometimes unphysical) perturbations with $\lambda \in [-25, 25]$, with a step $\Delta\lambda = 0.2$, truncating only when the bcc lattice became unstable. This yielded a total ensemble of around 20000 stable potentials. For each potential, we calculated the formation vacancy defect [37], allowing for relaxation of both structure and volume, meaning that only the full $ih+h$ expansion is expected to be asymptotically exact. The diversity of the resultant dataset allows for a robust test of our implicit Taylor expansions (36) and (7).

Figures 3a and 3b illustrate this approach. As expected, this form of perturbation applied to all stable potentials produced a wide range of very strong perturbations. Fig. 3c shows the formation volume error across the samples as a function of perturbation magnitude λ . Both homogeneous (h) and full ($h+ih$) expansions pro-

vide a nearly-perfect predictions of vacancy formation volume. However, for the formation energy, the full approach is notably more accurate, with errors under 2% across a wide (3 eV) range of formation energies (see Fig. 3d). This indicates that whilst the efficient homogeneous expansion offers a useful prediction of energy and volume changes, the inhomogeneous term allows for most accurate prediction at small to moderate perturbations. This asymptotic accuracy is particularly important when using the implicit derivative to solve inverse problems, which we discuss in the next section.

H. Implicit loss minimization applied to solute-induced dislocation core reconstruction

In this final section we employ the implicit derivative concept to solve a challenging inverse problem: with a starting potential Θ , and some stationary configurations \mathbf{X}_{Θ}^* , we search for the potential parameters that stabilize a structure as close as possible to some target configuration $\mathbf{X}_{\text{ref}}^*$. The ability to find parameters that yield certain desired structures represents a first step towards a range of inverse design strategies, in particular, given the ability of emerging universal potential models to smoothly interpolate across chemical space [20].

To demonstrate minimization of the implicit loss function (equation (9)), we selected a computationally challenging system of a ~ 2000 -atom tungsten disk with a $\langle 111 \rangle / 2$ screw dislocation along the disk axis, as illustrated on Fig. 4a. Using initial potential parameters Θ_0 for W from Goryaeva *et al.* [8], the dislocation core relaxes into the ‘easy’ core structure in agreement with *ab initio*. For the inverse problem, we assign one ‘alchemical’ atom (the red atom in Fig. 4a) with it’s own

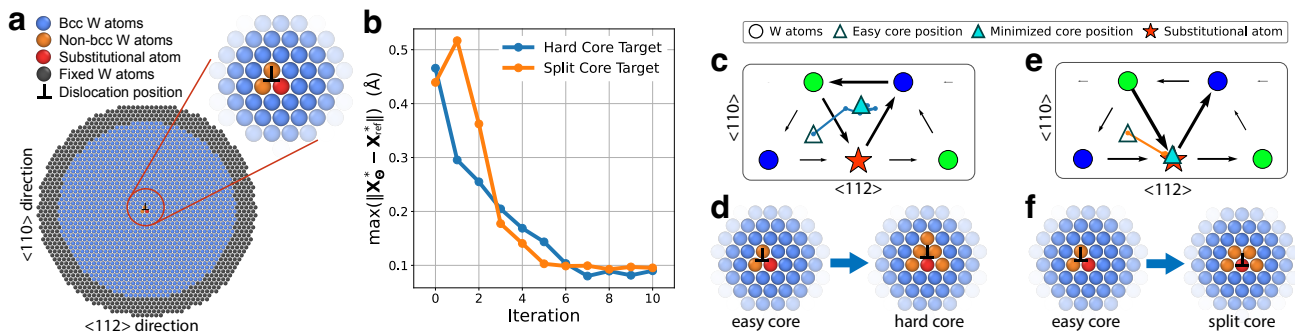


FIG. 4. **Targeting dislocation core reconstruction in tungsten.** **a** Dislocation cluster supercell. The ~ 2000 -atom cell has fixed boundary conditions in the $\langle 110 \rangle$ and $\langle 112 \rangle$ directions and periodic boundary conditions in the $\langle 111 \rangle$ direction with one Burgers vector within the cell. The ‘substitutional’ atom at the dislocation core (in red), initially has interaction parameters corresponding to tungsten, which vary during the loss minimization procedure. Around 500 atoms are fixed at the cluster border to stabilize the dislocation core structure [4]. Non-bcc atoms are identified using the OVITO package [38]. **b** Maximal difference of atomic positions between a current and the target configurations during the loss minimization procedure for target configurations set to ‘hard’ and ‘split’ cores. **c, e** Differential displacement maps [39] corresponding to final configurations of the minimization. The starting configuration for both simulations is the ‘easy’ core and the target configurations are the ‘hard’ core (**c**) and ‘split’ core (**e**). Transient dislocation core positions during the minimization are presented with lines starting at empty and ending at solid triangles, that depict initial and final core positions. **d, f** Atomic configurations around the dislocation core with ‘hard’ core (**d**) and ‘split’ core (**f**) target configurations.

independent set of parameters Θ , initially set to Θ_0 . We use a simple form for the linear multi-specie potential, detailed in the methods, section IV B. Modifying the alchemical potential parameters Θ whilst keeping Θ_0 fixed, we aim to stabilize the ‘hard’ and ‘split’ core structures, which are unstable for W [8, 40]. We monitor the effective dislocation core position during the minimization using the strain-matching approach detailed in [4]. The implicit loss minimization is achieved through the procedure presented in Algorithm 1, where the loss gradient is computed according to equation (10). We employ an adaptive step size h as detailed in supplementary material.

Algorithm 1 Implicit Loss Minimization

```

 $\Theta^{(0)} \leftarrow$  initial potential
 $\mathbf{X}_{\Theta^{(0)}}^* \leftarrow$  initial relaxed positions
 $k \leftarrow 0$ 
while  $k \leq$  max_interactions do
  Compute implicit derivative  $\nabla_{\Theta} \mathbf{X}_{\Theta^{(k)}}^*$ 
  Compute  $\nabla_{\Theta} L(\Theta^{(k)})$ 
   $\Theta^{(k+1)} \leftarrow \Theta^{(k)} - h \nabla_{\Theta} L(\Theta^{(k)})$ 
   $\mathbf{X}_{\Theta^{(k+1)}}^* \leftarrow \mathbf{X}_{\Theta^{(k)}}^* + (\Theta^{(k+1)} - \Theta^{(k)}) \nabla_{\Theta} \mathbf{X}_{\Theta^{(k)}}^*$ 
  if  $\|\mathbf{X}_{\Theta^{(k+1)}}^* - \mathbf{X}_{\Theta^{(k)}}^*\|_{\infty} < \varepsilon$  then
    return  $\mathbf{X}_{\Theta^{(k+1)}}^*, \Theta^{(k+1)}$ 
  end if
end while

```

Figure 4b shows the maximal deviation of atomic positions at iteration k for two target structures. The minimization error decreases significantly at first steps and saturates at ~ 10 iterations for both structures. The error does not reach zero, which we attribute to the target configurations being derived from pure tungsten sys-

tems, whereas our minimization involves systems that more closely represent substitutional defects. However, the minimization goals are clearly achieved as seen in Figure 4 panels c-f: the ‘hard’ core (Fig. 4c,d) and ‘split’ core (Fig. 4e,f) are located at expected positions denoted by solid triangles.

As a final application, we show how the implicit loss minimization can be used to fine-tune an initial interatomic potential to match *ab initio* training data. Here, our target is a solute-induced reconstruction of the $\langle 111 \rangle / 2$ screw dislocation core caused by an interstitial Be atom, using the same disk geometry as described above and shown in Fig. 5a. The target data was generated using the QM/ML simulation method which embeds a DFT region at core as detailed in methods IV C. As shown in Fig. 5b, we see that Be induces reconstruction to the ‘hard’ core structure, with the Be interstitial sitting at the center of the dislocation.

Using W-Be *ab initio* training data from Wood *et al.* [41], we created an initial set of Be interaction parameters Θ using the same linear multi-species interatomic potential as above (see methods, section IV B) with W parameters Θ_0 set to those from Goryaeva *et al.* [8]. The relaxed structure using the initial potential fit is shown in Fig. 5c. It can be seen that in contrast to the QM/ML target, the dislocation core remains in the ‘easy’ configuration, with the Be atom lying outside of the central core region. Using the procedure described above, we performed implicit loss minimization using this initial relaxed configuration. The implicit loss achieved near-perfect reproduction of the core reconstruction in around 20 iterations (see Fig. 5d and supplementary material).

III. DISCUSSION

In this paper, we have investigated the use of the implicit derivative of the relaxed atomic structure with interatomic potential parameters, giving a first-order implicit Taylor expansion for the relaxed structures and second-order for relaxed energies. We detailed how the implicit derivative could be calculated using dense linear algebra, requiring Hessian evaluation, automatic differentiation, or a Hessian-free linear operator approach, which reduces to a constrained minimization in LAMMPS, allowing application to arbitrarily large systems.

The implicit expansion enables very efficient forward propagation of parameter uncertainties to simulation results, including the effect of geometry relaxation, essential to capture changes in structure. This was demonstrated on simple classical models and machine learning models for pure tungsten. The implicit expansion was able to capture a wide range of changes in energy and structure, far beyond typical variations associated with potential parameter uncertainty. Beyond uncertainty quantification, our results show that the implicit expansion can also be used to rapidly explore the parameter space of high dimensional interatomic models, permitting parametric studies that would be intractable with standard methods. In future work, we will explore how the implicit expansion can be used in a correlative study of defect structures and implications for both uncertainty quantification and materials design goals.

In addition to the forward propagation enabled by the implicit expansion, we also investigated the use of the implicit derivative in backpropagation of structural changes to changes in potential parameters. Our exploratory applications focused on solute-induced dislocation core reconstruction in tungsten, a key feature in understanding plasticity and irradiation damage in bcc metals [42]. We showed how the implicit derivative could be used to ‘fine-tune’ parameters from an initial fit against training data for tungsten-beryllium, in order to stabilize the structure seen in *ab initio* calculations.

In a first effort towards targeted ‘alchemical’ design applications, we used the implicit derivative to find substitutional solute interaction parameters which stabilized ‘hard’ or ‘split’ dislocation cores in pure tungsten. The success of this effort extends the scope of alchemical machine learning to large-scale simulations essential for mechanistic studies of e.g. plasticity. We anticipate that both approaches will gain ever-increasing application with the advent of general-purpose ‘universal’ machine learning potentials, which will be a focus of future efforts.

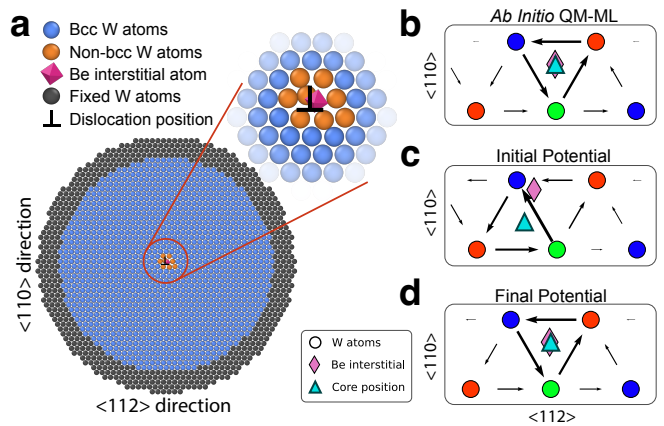


FIG. 5. ‘Fine-tuning’ Be-induced dislocation core reconstruction in tungsten. **a** Dislocation cluster supercell similar to that shown in figure 4, but with a Be interstitial in the center of the cluster and no substitution. **b**, **c**, **d** differential displacement maps [39] with dislocation core and interstitial positions corresponding to the QM-ML configuration (panel **b**), initial SNAP potential (panel **c**), and the minimum of the ‘fine-tuned’ potential (panel **d**).

IV. METHODS

A. Implementation of the sparse linear operator as a constrained minimization in LAMMPS

Equation (8) defines a linear operator which can be used in iterative solution of the linear equations (5) and thus to evaluate the implicit derivative $\nabla_{\Theta} \tilde{\mathbf{X}}_{\Theta}^*$. To fully exploit the efficiencies afforded by the Hessian sparsity, in this section, we detail how $\nabla_{\Theta} \tilde{\mathbf{X}}_{\Theta}^*$ can be implemented in the massively parallel LAMMPS simulation package. This is achieved through N_D constrained minimizations, one for each row $[\nabla_{\Theta} \tilde{\mathbf{X}}_{\Theta}^*]_l$, $l \in [1, N_D]$ of the implicit derivative. As follows from equations (5), the inhomogeneous term $\nabla_{\Theta} \tilde{\mathbf{X}}_{\Theta}^*$ satisfies

$$[\nabla_{\Theta} \tilde{\mathbf{X}}_{\Theta}^*]_l \nabla_{\tilde{\mathbf{X}}}^2 U + [\mathbf{B}]_l = 0, \quad (14)$$

where $\mathbf{B} = \nabla_{\Theta} \epsilon_{\Theta}^* \otimes \nabla_{\tilde{\mathbf{X}}}^2 U + \nabla_{\Theta}^2 U \in \mathbb{R}^{N_D \times N \times 3}$. For the linear-in-descriptor SNAP potentials used here, the $\nabla_{\Theta}^2 U$ term can be directly accessed as derivatives of descriptors [29] using `fix sna/atom` and related commands in LAMMPS. For the inverse design applications in this paper, which modified only the interaction parameters of a single solute atom without changes to the supercell strain, we have $\nabla_{\Theta} \epsilon_{\Theta}^* = \mathbf{0}$ and thus $\mathbf{B} = \nabla_{\Theta}^2 U$. With an initial parameter vector Θ , we then define the modified energy function for a parameter index l

$$U(\tilde{\mathbf{X}}, \mathbf{C}; \Theta) + \alpha [\mathbf{B}]_l \cdot [\tilde{\mathbf{X}} - \tilde{\mathbf{X}}_{\Theta}^*]. \quad (15)$$

This modified energy is simple to implement in LAMMPS through the `fix addforce` function, with similar ease of implementation in any molecular dynamics package.

In the limit $\alpha \rightarrow 0$, the minimizer $\tilde{\mathbf{X}}_{l,\alpha}^*$ of (15) gives the l^{th} vector $[\nabla_{\Theta} \tilde{\mathbf{X}}_{\Theta}^*]_l$ of the implicit derivative $\nabla_{\Theta} \tilde{\mathbf{X}}_{\Theta}^*$ through

$$[\nabla_{\Theta} \tilde{\mathbf{X}}_{\Theta}^*]_l = (\tilde{\mathbf{X}}_{l,\alpha}^* - \tilde{\mathbf{X}}_{\Theta}^*)/\alpha. \quad (16)$$

Further details regarding hyperparameter scanning for suitable values of α and comparison against the full dense linear solution employing the Hessian matrix is provided in supplementary material.

B. Multi-specie ML potentials

For systems with multiple atomic species $s_i \in [1, N_S]$, as investigated in sections II G, II H, we simply assign a new specie-dependent parameter vector as in the original SNAP paper [29], giving a total energy

$$U(\tilde{\mathbf{X}}, \mathbf{C}; \Theta) = \sum_i [\Theta]_{s_i} \mathbf{D}(\tilde{\mathbf{X}}, \mathbf{C}, i) \equiv \Theta \cdot \mathbf{D}(\tilde{\mathbf{X}}, \mathbf{C}), \quad (17)$$

where $\Theta \in \mathbb{R}^{N_S \times N_D}$ is the total parameter vector, $s_i \in [1, N_S]$ and $\mathbf{D}(\tilde{\mathbf{X}}, \mathbf{C}) \in \mathbb{R}^{N_S \times N_D}$ is the total descriptor vector. In typical usage practice, the descriptor functions have specie-dependent hyperparameters which must also be tuned, but here we assume these are fixed.

C. *Ab initio* QM-ML calculations

The *ab initio* reference data for Be segregation to screw dislocations in W was calculated using QM-ML hybrid simulations [4, 40], which couple *ab initio* and machine learning potentials. Initial structures were obtained with `matscipy.dislocation` module [43]. The Be segregation calculation used the same approach as for He segregation reported in [4]. *Ab initio* forces were evaluated using VASP [44, 45] with 10 \mathbf{k} -points along the periodic line direction, with a cutoff energy of 500 eV and a minimization force threshold of 0.01 eV/Å. The machine

learning force field was a modified SNAP/MILaDy potential from [8]. The QM/ML coupling used a buffer radius of 10 Å, resulting in a total of 246 VASP atoms, of which 168 were in the buffer.

V. DATA AVAILABILITY

The implicit derivative implementations derived will be publicly available on GitHub following peer review.

VI. ACKNOWLEDGEMENTS

IM and TDS gratefully acknowledge support from an Emergence@INP grant from the CNRS. TDS thanks the Institute for Pure and Applied Mathematics at the University of California, Los Angeles (supported by NSF grant DMS-1925919) for their hospitality. TDS and PG gratefully acknowledge support from ANR grants ANR-19-CE46-0006-1 and ANR-23-CE46-0006-1, IDRIS allocation A0120913455.

VII. CONTRIBUTIONS

TDS designed the research program and derived the initial theoretical results. IM implemented the sparse operator, designed the implicit loss minimizer, and ran all simulations. PG generated the dislocation structures and performed the QM/ML calculations. IM and TDS wrote the paper.

VIII. COMPETING INTERESTS

The authors declare no competing interests.

-
- [1] Van Der Giessen, E. *et al.* Roadmap on multiscale materials modeling. *Modelling and Simulation in Materials Science and Engineering* **28**, 043001 (2020).
 - [2] Deringer, V. L., Caro, M. A. & Csányi, G. Machine learning interatomic potentials as emerging tools for materials science. *Adv. Mater.* **31**, 1902765 (2019).
 - [3] Swinburne, T. & Perez, D. Automated calculation and convergence of defect transport tensors. *Npj Comput. Mater.* **6**, 190 (2020).
 - [4] Grigorev, P., Goryaeva, A. M., Marinica, M.-C., Kermode, J. R. & Swinburne, T. D. Calculation of dislocation binding to helium-vacancy defects in tungsten using hybrid *ab initio*-machine learning methods. *Acta Mater.* **247**, 118734 (2023).
 - [5] Wales, D. J. *Energy Landscapes* (Cambridge, 2003).
 - [6] Proville, L., Rodney, D. & Marinica, M.-C. Quantum effect on thermally activated glide of dislocations. *Nat. Mater.* **11**, 845–849 (2012).
 - [7] Goodrich, C. P., King, E. M., Schoenholz, S. S., Cubuk, E. D. & Brenner, M. P. Designing self-assembling kinetics with differentiable statistical physics models. *Proc. Natl. Acad. Sci. U.S.A.* **118**, e2024083118 (2021).
 - [8] Goryaeva, A. M. *et al.* Efficient and transferable machine learning potentials for the simulation of crystal defects in bcc Fe and W. *Phys. Rev. Mater.* **5**, 103803 (2021).
 - [9] Swinburne, T. D. & Perez, D. Parameter uncertainties for imperfect surrogate models in the low-noise regime (2024). 2402.01810.

- [10] Musil, F., Willatt, M. J., Langovoy, M. A. & Ceriotti, M. Fast and accurate uncertainty estimation in chemical machine learning. *J. Chem. Theory Comput.* **15**, 906–915 (2019).
- [11] George, E. P., Raabe, D. & Ritchie, R. O. High-entropy alloys. *Nat. Rev. Mater.* **4**, 515–534 (2019).
- [12] Zhou, Z. *et al.* Machine learning guided appraisal and exploration of phase design for high entropy alloys. *Npj Comput. Mater.* **5** (2019).
- [13] Ha, M.-Q. *et al.* Evidence-based recommender system for high-entropy alloys. *Nat. Comput. Sci.* **1**, 470–478 (2021).
- [14] Giuntoli, A. *et al.* Systematic coarse-graining of epoxy resins with machine learning-informed energy renormalization. *Npj Comput. Mater.* **7** (2021).
- [15] Banik, S. *et al.* A continuous action space tree search for inverse design (casting) framework for materials discovery. *Npj Comput. Mater.* **9** (2023).
- [16] Thaler, S., Stupp, M. & Zavadlav, J. Deep coarse-grained potentials via relative entropy minimization. *J. Chem. Phys.* **157** (2022).
- [17] Batatia, I., Kovács, D. P., Simm, G. N., Ortner, C. & Csányi, G. Mace: Higher order equivariant message passing neural networks for fast and accurate force fields. *arXiv preprint arXiv:2206.07697* (2022).
- [18] Batatia, I. *et al.* A foundation model for atomistic materials chemistry (2024). 2401.00096.
- [19] Deng, B. *et al.* Overcoming systematic softening in universal machine learning interatomic potentials by fine-tuning (2024). 2405.07105.
- [20] Nam, J. & Gomez-Bombarelli, R. Interpolation and differentiation of alchemical degrees of freedom in machine learning interatomic potentials (2024). 2404.10746.
- [21] Schoenholz, S. & Cubuk, E. D. Jax md: a framework for differentiable physics. *Adv. Neural Inf. Process. Syst.* **33**, 11428–11441 (2020).
- [22] Ablin, P., Peyré, G. & Moreau, T. Super-efficiency of automatic differentiation for functions defined as a minimum. In *International Conference on Machine Learning*, 32–41 (PMLR, 2020).
- [23] Blondel, M. *et al.* Efficient and modular implicit differentiation. *Adv. Neural Inf. Process. Syst.* **35**, 5230–5242 (2022).
- [24] Liu, H. *et al.* End-to-end differentiability and tensor processing unit computing to accelerate materials’ inverse design. *Npj Comput. Mater.* **9** (2023).
- [25] Krantz, S. G. & Parks, H. R. *The implicit function theorem: history, theory, and applications* (Springer Science & Business Media, 2002).
- [26] Plimpton, S. Fast Parallel Algorithms for Short-Range Molecular Dynamics. *J. Comput. Phys.* **117**, 1–19 (1995).
- [27] Xie, S. R., Rupp, M. & Hennig, R. G. Ultra-fast interpretable machine-learning potentials. *Npj Comput. Mater.* **9**, 162 (2023).
- [28] Del Masto, A., Baccou, J., Tréglia, G., Ribeiro, F. & Varvenne, C. Insights on the capabilities and improvement ability of classical many-body potentials: Application to α -zirconium. *Comput. Mater. Sci.* **231**, 112544 (2024).
- [29] Thompson, A. P., Swiler, L. P., Trott, C. R., Foiles, S. M. & Tucker, G. J. Spectral neighbor analysis method for automated generation of quantum-accurate interatomic potentials. *J. Comp. Phys.* **285**, 316 (2015).
- [30] Allen, A. E., Dusson, G., Ortner, C. & Csányi, G. Atomic permutationally invariant polynomials for fitting molecular force fields. *Mach. Learn.: Sci. Technol.* **2**, 025017 (2021).
- [31] Podryabinkin, E. V. & Shapeev, A. V. Active learning of linearly parametrized interatomic potentials. *Comput. Mater. Sci.* **140**, 171–180 (2017).
- [32] Lysogorskiy, Y. *et al.* Performant implementation of the atomic cluster expansion (PACE) and application to copper and silicon. *Npj Comput. Mater.* **7**, 1–12 (2021).
- [33] Batzner, S. *et al.* E (3)-equivariant graph neural networks for data-efficient and accurate interatomic potentials. *Nat. Commun.* **13**, 1–11 (2022).
- [34] Reali, L., Boleininger, M., Gilbert, M. R. & Dudarev, S. L. Macroscopic elastic stress and strain produced by irradiation. *Nucl. Fusion* **62**, 016002 (2021).
- [35] Bartók, A. P., Payne, M. C., Kondor, R. & Csányi, G. Gaussian approximation potentials: The accuracy of quantum mechanics, without the electrons. *Phys. Rev. Lett.* **104**, 136403 (2010).
- [36] Bartók, A. P. *et al.* Machine learning unifies the modeling of materials and molecules. *Sci. Adv.* **3**, e1701816 (2017).
- [37] Ashcroft, N. W. & Mermin, N. D. *Solid State Physics* (Holt-Saunders, Fort Worth, TX, 1976).
- [38] Stukowski, A. Visualization and analysis of atomistic simulation data with ovito—the open visualization tool. *Model. Simul. Mat. Sci. Eng.* **18**, 015012 (2009).
- [39] Vitek, V. Theory of the core structures of dislocations in body-centred-cubic metals. *Cryst. Latt. Def. Amorp.* (1974).
- [40] Grigorev, P., Swinburne, T. D. & Kermode, J. R. Hybrid quantum/classical study of hydrogen-decorated screw dislocations in tungsten: Ultrafast pipe diffusion, core reconstruction, and effects on glide mechanism. *Physical Review Materials* **4** (2020).
- [41] Wood, M. A., Cusentino, M. A., Wirth, B. D. & Thompson, A. P. Data-driven material models for atomistic simulation. *Phys. Rev. B* **99**, 184305 (2019).
- [42] Hachet, G., Ventelon, L., Willaime, F. & Clouet, E. Screw dislocation-carbon interaction in bcc tungsten: an ab initio study. *Acta Mater.* **200**, 481–489 (2020).
- [43] Grigorev, P. *et al.* matscipy: materials science at the atomic scale with python. *J. Open Source Softw.* **9**, 5668 (2024).
- [44] Kresse, G. & Furthmüller, J. Efficient iterative schemes for ab initio total-energy calculations using a plane-wave basis set. *Phys. Rev. B* **54**, 11169–11186 (1996).
- [45] Perdew, J. P., Burke, K. & Ernzerhof, M. Generalized gradient approximation made simple. *Phys. Rev. Lett.* **77**, 3865–3868 (1996).

Supplemental Material for: Exploring the parameter dependence of atomic minima with implicit differentiation

1. IMPLICIT DIFFERENTIATION

A. General expression derivation

Here we consider \mathbf{X}_Θ^* as a stationary configuration that includes the scaled atomic coordinates $\tilde{\mathbf{X}}_\Theta^*$ and supercell \mathbf{C}_Θ^* . A stationary configuration is defined with a zero-force condition:

$$\mathbf{F}(\mathbf{X}_\Theta^*; \Theta) = \mathbf{0}. \quad (18)$$

Under a parameter perturbation, $\Theta + \delta\Theta$, a new stationary configuration $\mathbf{X}_{\Theta+\delta\Theta}^*$ will satisfy:

$$\mathbf{F}(\mathbf{X}_{\Theta+\delta\Theta}^*; \Theta + \delta\Theta) = \mathbf{0}. \quad (19)$$

Hence, under a parameter perturbation, the differential of the force is zero as well:

$$d\mathbf{F}(\mathbf{X}_{\Theta+\delta\Theta}^*; \Theta + \delta\Theta) = \delta\mathbf{X}_\Theta^* \nabla_{\mathbf{X}} \mathbf{F}(\mathbf{X}_\Theta^*; \Theta) + \delta\Theta \cdot \nabla_{\Theta} \mathbf{F}(\mathbf{X}_\Theta^*; \Theta) + \mathcal{O}(\delta\Theta^2) = \mathbf{0}. \quad (20)$$

We express the variation in coordinates using the implicit derivative definition $\delta\mathbf{X}_\Theta^* = \delta\Theta \nabla_{\Theta} \mathbf{X}_\Theta^*$ and obtain

$$\delta\Theta \cdot [\nabla_{\Theta} \mathbf{X}_\Theta^* \nabla_{\mathbf{X}} \mathbf{F}(\mathbf{X}_\Theta^*; \Theta) + \nabla_{\Theta} \mathbf{F}(\mathbf{X}_\Theta^*; \Theta)] = \mathbf{0} + \mathcal{O}(\delta\Theta^2). \quad (21)$$

As this holds for any parameter variation $\delta\Theta$, the term inside the square brackets is zero. Finally, we will express the force through energy $U(\mathbf{X}_\Theta^*; \Theta) = -\nabla_{\mathbf{X}} \mathbf{F}(\mathbf{X}_\Theta^*; \Theta)$ and get

$$\nabla_{\Theta} \mathbf{X}_\Theta^* \nabla_{\mathbf{X}\mathbf{X}}^2 U(\mathbf{X}_\Theta^*; \Theta) = -\nabla_{\Theta \mathbf{X}} U(\mathbf{X}_\Theta^*; \Theta). \quad (22)$$

Expressing atomic coordinates as $\mathbf{X} = \tilde{\mathbf{X}}\mathbf{C}$ and splitting the position and mixed Hessians on the scaled coordinate, off-diagonal, and supercell blocks, $(\nabla_{\tilde{\mathbf{X}}\tilde{\mathbf{X}}}^2 U)$, $(\nabla_{\tilde{\mathbf{X}}\epsilon}^2 U)$, $(\nabla_{\epsilon\epsilon}^2 U)$, one gets the equation (5) from the main text.

B. Homogeneous implicit derivative of strain

In this work, we split the full implicit derivative (equation (22)) onto the *inhomogeneous* and *homogeneous* contributions. As explained in the main text (methods A), the *inhomogeneous* implicit derivative $\nabla_{\Theta} \tilde{\mathbf{X}}_\Theta^*$ can be computed in LAMMPS with constraint minimization, or alternatively, with automatic differentiation (AD), section IID from the main text. Here, we detail our finite difference implementation of the *homogeneous* part of the implicit derivative, $\nabla_{\Theta} \epsilon_\Theta^*$.

A stationary configuration of a system of volume V_Θ^* corresponds to zero pressure:

$$P(V_\Theta^*) = - \left. \frac{\partial U(\tilde{\mathbf{X}}_\Theta^*, \mathbf{C}_\Theta^*; \Theta)}{\partial V} \right|_{V_\Theta^*} = 0. \quad (23)$$

For isotropic supercell variations, $\mathbf{C}_\Theta^* = [1 + \epsilon_\Theta^*] \mathbf{C}_0$, this equation can be reformulated in terms of strain:

$$\left. \frac{\partial U(\tilde{\mathbf{X}}, \epsilon; \Theta)}{\partial \epsilon} \right|_{\tilde{\mathbf{X}}_\Theta^*, \epsilon_\Theta^*} = 0. \quad (24)$$

In this section, we neglect the *inhomogeneous* contribution to the strain derivative and we will omit $\tilde{\mathbf{X}}$ from the arguments of U for clarity. For linear-in-descriptor potentials (e.g. equation (12) in the main text), equation (24) writes

$$\Theta \cdot \left. \frac{\partial \mathbf{D}(\epsilon)}{\partial \epsilon} \right|_{\epsilon_\Theta^*} = 0. \quad (25)$$

Note that the descriptor vector does not depend on potential parameters Θ . In analogy with the previous section (equation (20)), we consider a system upon a parameter variation $\Theta + \delta\Theta$:

$$\left. \frac{\partial U(\epsilon; \Theta + \delta\Theta)}{\partial \epsilon} \right|_{\epsilon_{\Theta}^* + \delta\epsilon_{\Theta}^*} = 0. \quad (26)$$

Applying the linear-in-descriptor form of potential energy, we get:

$$(\Theta + \delta\Theta) \cdot \left. \frac{\partial \mathbf{D}(\epsilon)}{\partial \epsilon} \right|_{\epsilon_{\Theta}^* + \delta\epsilon_{\Theta}^*} = 0. \quad (27)$$

Neglecting the term proportional to $\delta\Theta\delta\epsilon_{\Theta}^*$, we get

$$\delta\Theta \cdot \left. \frac{\partial \mathbf{D}(\epsilon)}{\partial \epsilon} \right|_{\epsilon_{\Theta}^*} + \delta\epsilon_{\Theta}^* \Theta \cdot \left. \frac{\partial^2 \mathbf{D}(\epsilon)}{\partial \epsilon^2} \right|_{\epsilon_{\Theta}^*} = 0. \quad (28)$$

We then use the definition of the *homogeneous* implicit derivative, $\delta\epsilon_{\Theta}^* = \delta\Theta \nabla_{\Theta} \epsilon_{\Theta}^*$:

$$\delta\Theta \cdot \left[\left. \frac{\partial \mathbf{D}(\epsilon)}{\partial \epsilon} + \nabla_{\Theta} \epsilon_{\Theta}^* \left(\Theta \cdot \frac{\partial^2 \mathbf{D}(\epsilon)}{\partial \epsilon^2} \right) \right]_{\epsilon_{\Theta}^*} = 0. \quad (29)$$

Since this equation is valid for any parameter variation $\delta\Theta$, we can get the final expression for the *homogeneous* implicit derivative:

$$\nabla_{\Theta} \epsilon_{\Theta}^* = - \left. \frac{\partial \mathbf{D}(\epsilon)/\partial \epsilon}{\Theta \cdot \partial^2 \mathbf{D}(\epsilon)/\partial \epsilon^2} \right|_{\epsilon_{\Theta}^*}. \quad (30)$$

For numerical purposes, we evaluate the derivatives of the descriptor vector with finite differences:

$$\frac{\partial \mathbf{D}(\epsilon_{\Theta}^*)}{\partial \epsilon} \approx \frac{\mathbf{D}(\epsilon_{\Theta}^* + \Delta\epsilon) - \mathbf{D}(\epsilon_{\Theta}^* - \Delta\epsilon)}{2\Delta\epsilon}; \quad \frac{\partial^2 \mathbf{D}(\epsilon_{\Theta}^*)}{\partial \epsilon^2} \approx \frac{\mathbf{D}(\epsilon_{\Theta}^* + \Delta\epsilon) + \mathbf{D}(\epsilon_{\Theta}^* - \Delta\epsilon) - 2\mathbf{D}(\epsilon_{\Theta}^*)}{\Delta\epsilon^2}, \quad (31)$$

where $\Delta\epsilon$ is typically 10^{-3}\AA .

C. Implicit derivative of strain including *homogeneous* and *inhomogeneous* terms

Let us take into account the *inhomogeneous* contribution in equation (26):

$$\left. \frac{\partial U(\tilde{\mathbf{X}}_{\Theta}^* + \delta\tilde{\mathbf{X}}_{\Theta}^*, \epsilon_{\Theta}^* + \delta\epsilon_{\Theta}^*; \Theta + \delta\Theta)}{\partial \epsilon} \right|_{\epsilon_{\Theta}^* + \delta\epsilon_{\Theta}^*} = 0. \quad (32)$$

Following a similar procedure as in the previous section, we get the *h+ih* level of approximation for the strain implicit derivative:

$$\nabla_{\Theta} \epsilon_{\Theta}^* = - \left. \frac{\partial \mathbf{D}(\epsilon)/\partial \epsilon + \nabla_{\Theta} \mathbf{X}_{\Theta}^* \partial \mathbf{F}/\partial \epsilon}{\Theta \cdot \partial^2 \mathbf{D}(\epsilon)/\partial \epsilon^2} \right|_{\tilde{\mathbf{X}}_{\Theta}^*, \epsilon_{\Theta}^*}, \quad (33)$$

where the force derivative over the strain is evaluated with the finite difference approach.

D. Taylor expansion of energy

In this section, we derive the expansion of potential energy of a stationary system, $U(\mathbf{X}_{\Theta}^*; \Theta)$, under a potential parameter perturbation. For clarity, we will omit $(\mathbf{X}_{\Theta}^*; \Theta)$ from $U(\mathbf{X}_{\Theta}^*; \Theta)$ in this section. For the expansion, one has to account for contributions arising from the explicit dependence of U on parameters Θ , but also from the change in stationary configuration \mathbf{X}_{Θ}^* . Here, we first consider the general atomic coordinates \mathbf{X}_{Θ}^* and later split them on scaled coordinates $\tilde{\mathbf{X}}_{\Theta}^*$ and supercell \mathbf{C}_{Θ}^* .

Under a parameter perturbation $\Theta + \delta\Theta$, the potential energy expansion reads

$$\begin{aligned} U(\mathbf{X}_{\Theta}^* + \delta\mathbf{X}_{\Theta}^*; \Theta + \delta\Theta) &= U + \delta\mathbf{X}_{\Theta}^* \nabla_{\mathbf{X}} U + \delta\Theta \nabla_{\Theta} U \\ &+ \frac{1}{2} \delta\mathbf{X}_{\Theta}^* \nabla_{\mathbf{X}\mathbf{X}}^2 U \delta\mathbf{X}_{\Theta}^{*\top} + \frac{1}{2} \delta\Theta \nabla_{\Theta\Theta}^2 U \delta\Theta^{\top} + \delta\Theta \nabla_{\Theta\mathbf{X}}^2 U \delta\mathbf{X}_{\Theta}^{*\top} + \mathcal{O}(\delta\Theta^3) \end{aligned} \quad (34)$$

The term proportional to $\nabla_{\mathbf{X}} U$ vanishes since \mathbf{X}_{Θ}^* is a stationary atomic configuration. For the second-order terms, we express $\delta\mathbf{X}_{\Theta}^*$ using the implicit derivative: $\delta\mathbf{X}_{\Theta}^* = \delta\Theta \nabla_{\Theta} \mathbf{X}_{\Theta}^*$. We further use the implicit derivative expression, equation (22), and get: $\delta\mathbf{X}_{\Theta}^* = -\delta\Theta \nabla_{\Theta\mathbf{X}}^2 U [\nabla_{\mathbf{X}\mathbf{X}}^2 U]^{\dagger}$. The final energy expansion up to terms $\mathcal{O}(\delta\Theta^3)$ reads:

$$U(\mathbf{X}_{\Theta}^* + \delta\mathbf{X}_{\Theta}^*; \Theta + \delta\Theta) = U + \delta\Theta \nabla_{\Theta} U + \frac{1}{2} \delta\Theta \left[\nabla_{\Theta\Theta}^2 U + \nabla_{\Theta\mathbf{X}}^2 U (\nabla_{\Theta} \mathbf{X}_{\Theta}^*)^{\top} \right] \delta\Theta^{\top}. \quad (35)$$

In the main text, we outline the energy expansion as follows:

$$\delta^{(\zeta)} U^* \equiv \delta\Theta \nabla_{\Theta} U + \delta\Theta \mathbf{H}_{\zeta} \delta\Theta^{\top} + \mathcal{O}(\delta\Theta^3), \quad (36)$$

where ζ represents the level of approximation. Considering $\mathbf{X} = \tilde{\mathbf{X}}\mathbf{C}$ and employing the implicit derivative definitions for scaled coordinates and strain, $\nabla_{\Theta} \tilde{\mathbf{X}}_{\Theta}^*$ and $\nabla_{\Theta} \epsilon_{\Theta}^*$ (equations (2)-(5) from the main text), we derive the expressions of \mathbf{H}_{ζ} corresponding to each level of approximation:

- *constant (c)*: $\mathbf{H}_c = \nabla_{\Theta\Theta}^2 U$
- *homogeneous (h)*: $\mathbf{H}_h = \nabla_{\Theta\Theta}^2 U + \nabla_{\Theta\epsilon}^2 U (\nabla_{\Theta} \epsilon_{\Theta}^*)^{\top}$
- *inhomogeneous (ih)*: $\mathbf{H}_{ih} = \nabla_{\Theta\Theta}^2 U + \nabla_{\Theta\tilde{\mathbf{X}}}^2 U (\nabla_{\Theta} \tilde{\mathbf{X}}_{\Theta}^*)^{\top}$.

2. EFFICIENCY OF IMPLICIT DERIVATIVE EVALUATION SCHEMES

In this section, we provide the details on memory and time efficiency of the automatic differentiation (AD) and LAMMPS implementations of the implicit derivative. Given its computational complexity, our focus here will be on the *inhomogeneous* contribution, $\nabla_{\Theta} \tilde{\mathbf{X}}_{\Theta}^*$.

A. Automatic differentiation implementation

Here, we use the LJ random fcc alloy (presented in the main text, section IIF) as a test system. We compute the implicit derivative with AD using three approaches: 1) Computing the pseudo-inverse of the Hessian matrix with dense linear algebra solution, called *dense*. 2) Finding $\mathbf{X}_{\Theta+\delta\Theta}^*$ with minimization (gradient descent method was used in this work) and applying AD to the entire pipeline of functions (potential energy and its derivatives) with `jaxopt` Python library, called *jaxopt*. 3) Sparse linear operator technique (section IIC in the main text) within the AD framework, called *sparse*.

For this study, we used the best-in-class NVIDIA A100 80 GB graphic card tailored for scientific computations. To track the usage of the GPU memory for each solver and system size, we used the NVIDIA Management Library, `nvml` through the Python interface provided by the `pynvml` package. Figure 6 shows the time (panel **a**) and memory (panel **b**) required for *inhomogeneous* implicit derivative evaluation as a function of number of atoms in the system.

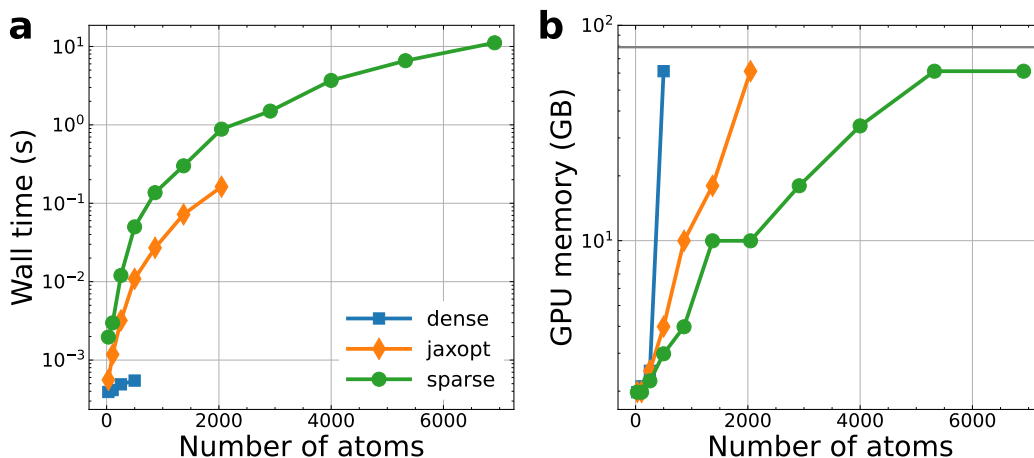


FIG. 6. **Efficiency of AD implicit derivative solvers.** **a** Wall time and **b** GPU memory required to compute the *inhomogeneous* implicit derivative vs the number of atoms in an LJ random alloy system. The gray horizontal line on panel **b** indicates the GPU memory limit of NVIDIA A100 80 GB graphic card.

The *inverse* approach shows the best time performance, however, it runs out of 80 GB GPU memory at a system of 500 atoms. The second fastest, *jaxopt* method, allows one to achieve system sizes of up to 2000 atoms before saturating the memory. Lastly, *sparse* technique, is the most memory efficient and reaches the systems of up to 7000 atoms on a single A100 GPU.

We would like to emphasize that while the methods based on AD provide unique advantages such as computational efficiency and ease of implementation, their substantial memory consumption significantly limits their applicability for large-scale simulations.

B. Implicit derivative implementation using LAMMPS package

Here, we discuss the time and memory efficiency of the *inhomogeneous* implicit derivative implementation using the LAMMPS software. The test system is a vacancy in bcc tungsten with SNAP potential (section IIG in the main text). We used four CPU nodes with two MD EPYC 7763 CPUs and 512 GB of RAM per node. We monitored RAM usage with the `vmstat` tool. We test the efficiency of the *dense* and *sparse* approaches presented above for AD. Additionally, we explore the efficiency of the constraint energy minimization approach, called *energy*, that is described in the main text (section IVA). As seen from Figure 7, the energy approach is the most time- and memory-efficient for large systems. Due to the efficient massive parallelization of the LAMMPS software, this method can be effectively scaled, allowing implicit derivative evaluation for systems of arbitrary size.

3. LAMMPS IMPLEMENTATION: ACCURACY AND NUMERICAL DETAILS

A. Accuracy of position change predictions

In this section, we present a comparison of three methods for evaluating the *inhomogeneous* implicit derivative, *dense*, *sparse*, and *energy*, as discussed above, implemented within the LAMMPS package. The test system is a vacancy in bcc tungsten and SNAP potential parameters are set according to the section IIG of the main text, equation (13), $\delta\Theta = \lambda(\Theta_m - \Theta)$, with a strong perturbation of $\lambda = 40$ and one selected potential sample m . The predicted position changes are computed as

$$\delta\tilde{\mathbf{X}}^{\text{pred}} = \tilde{\mathbf{X}}^* + \delta\Theta\nabla_{\Theta}\tilde{\mathbf{X}}_{\Theta}^*, \quad (37)$$

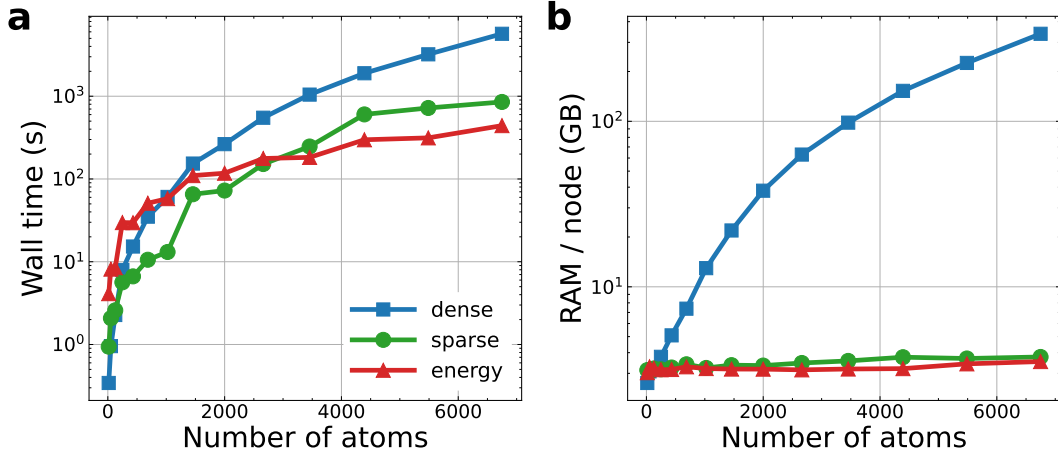


FIG. 7. **Efficiency of LAMMPS implicit derivative implementation approaches.** **a** Wall time and **b** RAM required to compute the *inhomogeneous* implicit derivative as a function of the number of atoms in a vacancy in a bcc tungsten system with SNAP potential.

where the *inhomogeneous* implicit derivative $\nabla_{\Theta} \tilde{\mathbf{X}}_{\Theta}^*$ is computed with one of the three method and positions $\tilde{\mathbf{X}}^*$ are obtained through the energy minimization of the system with the reference potential Θ . The true position changes are calculated as follows

$$\delta \tilde{\mathbf{X}}^{* \text{ true}} = \tilde{\mathbf{X}}^*(\Theta) - \tilde{\mathbf{X}}^*(\bar{\Theta}), \quad (38)$$

where $\tilde{\mathbf{X}}^*(\Theta)$ are the minimized positions of a system with parameters Θ using LAMMPS, the minimum image convention is applied to coordinates.

As shown in Fig. 8a, there is a remarkable agreement between the true and predicted positions, with negligible differences among the three computational methods. Given the low computational cost and memory requirements, the *energy* method stands out as the optimal choice for *inhomogeneous* implicit derivative evaluation.

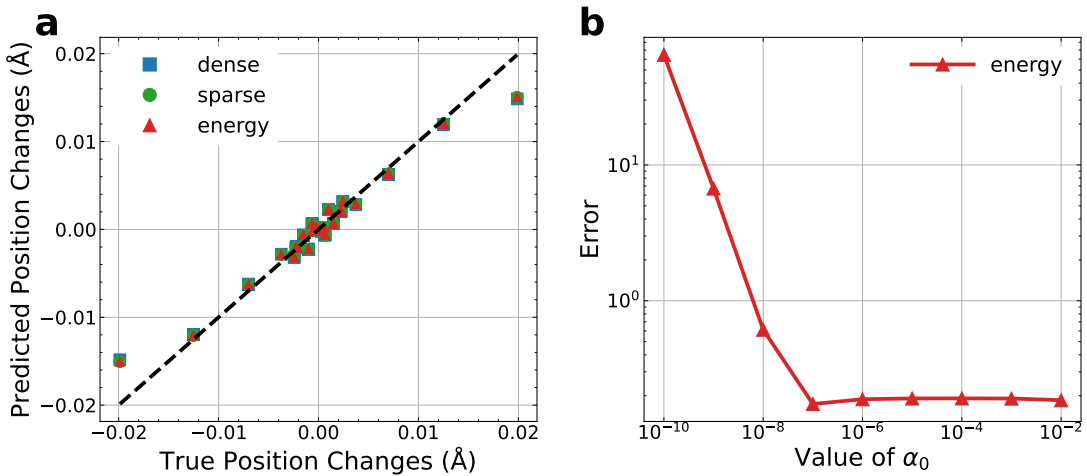


FIG. 8. **Accuracy of the *inhomogeneous* implicit derivative solvers implemented in LAMMPS.** **a** Predicted vs true position changes for the vacancy in the bcc tungsten system. **b** Error of the *inhomogeneous* position changes prediction for the *energy* method as a function of the α_0 parameter.

B. Numerical details of LAMMPS constraint energy minimization

Here, we detail our constraint energy minimization approach (called *energy*) to compute the *inhomogeneous* implicit derivative implemented in LAMMPS. As explained in the main text, the implicit derivative corresponding to a parameter index l is obtained as $[\nabla_{\Theta} \tilde{\mathbf{X}}_{\Theta}^*]_l = (\tilde{\mathbf{X}}_{l,\alpha}^* - \tilde{\mathbf{X}}_{\Theta}^*)/\alpha$. We have found that the optimal values of α should be computed for each parameter Θ_l separately as follows

$$\alpha(l) = \frac{\alpha_0}{\max(|[\nabla_{\Theta \tilde{\mathbf{X}}}^2 U]_l|)}, \quad (39)$$

where α_0 is a constant and $[\nabla_{\Theta \tilde{\mathbf{X}}}^2 U]_l$ is a row l of the mixed Hessian.

Figure 8b presents the dependence of the error of the implicit derivative prediction as a function of the α_0 parameter. The error is computed as

$$\frac{\|\delta \tilde{\mathbf{X}}^* \text{ true} - \delta \tilde{\mathbf{X}}^* \text{ pred}\|}{\|\delta \tilde{\mathbf{X}}^* \text{ true}\|}. \quad (40)$$

For $\alpha_0 < 10^{-7}$, the error is large due to limitations in machine precision. For larger α_0 values, the error does not change. However, the number of energy minimization iterations increases significantly for $\alpha_0 \geq 10^{-3}$. Therefore, we conclude that values of $\alpha_0 \in [10^{-6}; 10^{-4}]$ are optimal for the *energy* implicit derivative method. For the constraint energy minimization, we use the FIRE algorithm implemented in LAMMPS.

4. INVERSE DESIGN

A. Adaptive step for loss minimization

This section describes the adaptive step calculation for the inverse design applications. As explained in the main text (section IIIH), at iteration $k+1$ of the minimization procedure, the potential parameters are updated as $\Theta^{(k+1)} = \Theta^{(k)} - h \nabla_{\Theta} L(\Theta^{(k)})$ and positions as $\mathbf{X}_{\Theta^{(k+1)}}^* = \mathbf{X}_{\Theta^{(k)}}^* + (\Theta^{(k+1)} - \Theta^{(k)}) \nabla_{\Theta} \mathbf{X}_{\Theta^{(k)}}^* = \mathbf{X}_{\Theta^{(k)}}^* - h \nabla_{\Theta} L(\Theta^{(k)}) \nabla_{\Theta} \mathbf{X}_{\Theta^{(k)}}^*$. Accordingly, the loss at iteration $k+1$ is

$$L(\Theta^{(k+1)}) = \frac{1}{2} \|\mathbf{X}_{\Theta^{(k)}}^* + h \Delta \mathbf{X}_{\Theta^{(k)}}^{(0)} - \mathbf{X}_{\text{ref}}^*\|^2, \quad (41)$$

where $\Delta \mathbf{X}_{\Theta^{(k)}}^{(0)}$ is defined as the change in atomic positions corresponding to step $h = 1$, $\Delta \mathbf{X}_{\Theta^{(k)}}^{(0)} \equiv -\nabla_{\Theta} L(\Theta^{(k)}) \nabla_{\Theta} \mathbf{X}_{\Theta^{(k)}}^*$. Then, the *change* in loss at a given iteration is

$$\Delta L(\Theta^{(k+1)}) \equiv L(\Theta^{(k+1)}) - L(\Theta^{(k)}) = h \Delta \mathbf{X}_{\Theta^{(k)}}^{(0)\top} (\mathbf{X}_{\Theta^{(k)}}^* - \mathbf{X}_{\text{ref}}^*) + \frac{1}{2} h^2 \|\Delta \mathbf{X}_{\Theta^{(k)}}^{(0)}\|^2. \quad (42)$$

Finally, the step $h(k)$ that minimizes the loss at iteration k can be found as

$$h(k) = -\frac{\Delta \mathbf{X}_{\Theta^{(k)}}^{(0)\top} (\mathbf{X}_{\Theta^{(k)}}^* - \mathbf{X}_{\text{ref}}^*)}{\|\Delta \mathbf{X}_{\Theta^{(k)}}^{(0)}\|^2}. \quad (43)$$

Accordingly, the atomic position change at iteration $k+1$ is

$$\Delta \mathbf{X}_{\Theta^{(k)}} = h(k) \nabla_{\Theta} L(\Theta^{(k)}) \nabla_{\Theta} \mathbf{X}_{\Theta^{(k)}}^*. \quad (44)$$

B. W-Be Potential fine-tuning

Figure 9 presents the loss minimization for the potential fine-tuning for the W-Be system presented in the main text (section IIIH).

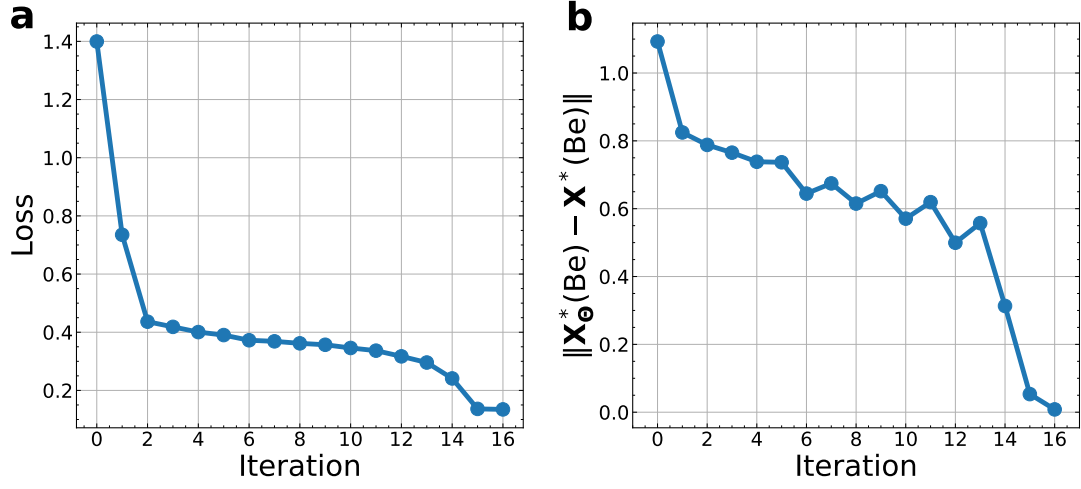


FIG. 9. **Loss minimization for W-Be potential fine-tuning.** **a** Implicit loss during the minimization procedure as defined in equation (9) of the main text. **b** Difference between a current and target Be atom positions during minimization.